

₁ Physics-Infused Reduced-Order Modeling for Analysis of
₂ Ablating Hypersonic Thermal Protection Systems

₃

₄ October 19, 2025

₅ **Abstract**

₆ This work presents a physics-infused reduced-order modeling (PIROM) framework
₇ towards the design, analysis, and optimization of non-decomposing ablating hypersonic
₈ thermal protection systems (TPS).

₉ **1 Introduction**

₁₀ At hypersonic speeds, aerospace vehicles experience extreme aero-thermal environments that
₁₁ requires specialized thermal protection systems (TPS) to shield internal sub-structures, elec-
₁₂ tronics, and possibly crew members from the intense aerodynamic heating. The TPS is often
₁₃ composed of ablating materials – a high-temperature capable fibrous material injected with
₁₄ a resin that fills the pore network and strengthens the composite [Amar2016](#). The TPS de-
₁₅ sign promotes the exchange of mass through thermal and chemical reactions (i.e., pyrolysis),
₁₆ effectively mitigating heat transfer to the sub-structures.

₁₇ As a result, accurate prediction for the ablating TPS response under extreme hypersonic
₁₈ heating becomes fundamental to ensuring survivability, performance, and safety of hyper-
₁₉ sonic vehicles. Not only is it necessary to assess the performance of the thermal management
₂₀ systems, but also the shape changes of the vehicle’s outer surface induced by the ablating
₂₁ material, and its impact on the aerodynamics, structural integrity, and controllability. Un-
₂₂ fortunately, high-fidelity simulations of ablating TPS remains a formidable challenge both
₂₃ theoretically and computationally.

₂₄ On the theoretical side, the thermo-chemical reactions, coupled with the irregular pore
₂₅ network structure, translate into simplifying assumptions to reduce non-linearities, and make
₂₆ the resulting equations more amenable for engineering application and design analysis [x](#).
₂₇ For instance, one of the most notable codes is the one-dimensional [CMA](#) code that was

28 developed by Aerotherm Corporation in the 1960s [Howard2015](#). Despite its practical use
29 in...

30 Another example is the CHarring Ablator Response (CHAR) ablation code, which ignores
31 elemental decompositions of the pyrolyzing gases, assumes the gases to be a mixture of perfect
32 gases in thermal equilibrium, and assumes no reaction or condensation with the porous
33 network [?].

34 theoretically:

35 computationally:

36 2 Modeling of Ablating Thermal Protection Systems

37 This section presents the problem of modeling ablation for a non-decomposing TPS as a
38 parametrized system of coupled non-linear PDEs. The ablation physics is decomposed into
39 heat conduction and mesh motion, which are governed by the energy and pseudo-elasticity
40 PDEs, respectively. Predictions for the ablating TPS response computed based on two
41 models: (1) a high-fidelity FOM based on discontinuous Galerkin FEM (DG-FEM), and (2)
42 an RPM based on the LCM. The mathematical details for the governing equations, FOM,
43 and RPM, are provided next.

44 2.1 Governing Equations

45 **Heat Conduction** Consider a generic domain $\Omega \subset \mathbb{R}^d$, $d = 2$ or 3 , illustrated in Fig. 1. Let
46 $\partial\Omega = \Gamma_q \cup \Gamma_T$ and $\Gamma_q \cap \Gamma_T = \emptyset$, where a Neumann $q_b(x, t)$ boundary condition is prescribed on
47 the Γ_q boundary, and a Dirichlet $T_b(x, t)$ boundary condition is prescribed on the boundary
48 Γ_T . The ablation is modeled as mesh motion, and occurs only on the heated boundary Γ_q .
49 Ablating effects on the energy equation are handled using the Arbitrary Lagrangian-Eulerian
50 (ALE) description. The ALE establishes that mesh displacements $w(x, t) \in \mathbb{R}^d$ and velocities
51 $v(x, t) \in \mathbb{R}^d$ evolve independently of the physical material's displacements, which are set to
52 zero [CITE](#).

53 The transient heat conduction is described by the energy equation,

$$54 \rho c_p \left(\frac{\partial T}{\partial t} - v(x, t) \cdot \nabla T \right) - \nabla \cdot (\mathbf{k} \nabla T) = \mathcal{Q}(x, t), \quad x \in \Omega \quad (1a)$$

$$55 -\mathbf{k} \nabla T \cdot \mathbf{n} = q_b(x, t), \quad x \in \Gamma_q \quad (1b)$$

$$56 T(x, t) = T_b(x, t), \quad x \in \Gamma_T \quad (1c)$$

$$57 T(x, 0) = T_0(x), \quad x \in \Omega \quad (1d)$$

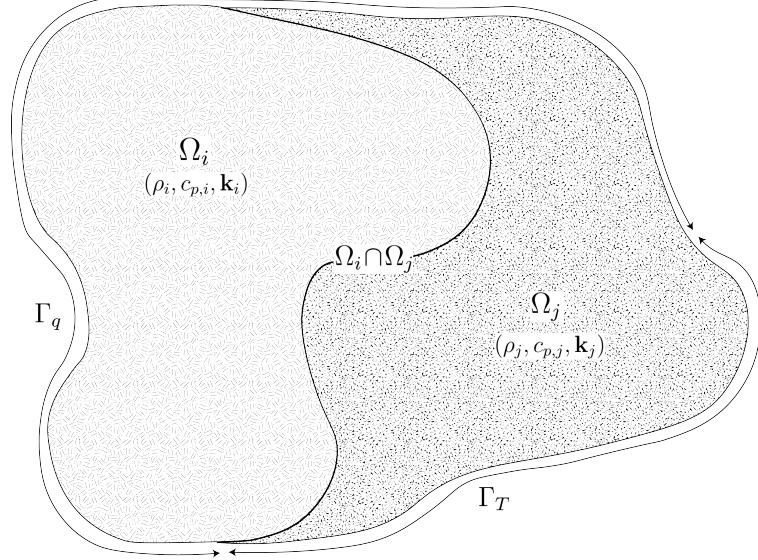


Figure 1: General domain Ω with prescribed Neumann and Dirichlet boundary conditions on Γ_q and Γ_T . Mesh displacement $w(x, t)$ occurs on the Γ_q boundary.

where the density ρ is constant, while the heat capacity c_p and thermal conductivity $\mathbf{k} \in \mathbb{R}^{d \times d}$, are temperature dependent. In the order they appear, the terms in eq. (1a) include, the unsteady energy storage, heat conduction, temperature advection due to mesh motion, and source terms due to boundary conditions. The boundary conditions for the energy equation includes Neumann eq. (1b) on Γ_1 and Dirichlet eq. (1c) on Γ_T .

Mesh Motion The mesh motion is described by the pseudo-elasticity equation,

$$\nabla \cdot \sigma(w) = 0 \quad (2a)$$

$$w(x, t) = w_q(x, t), \quad x \in \Gamma_q \quad (2b)$$

$$w(x, t) = 0, \quad x \notin \Gamma_q \quad (2c)$$

$$w(x, 0) = \mathbf{0} \quad (2d)$$

where the stress tensor σ is related to the strain tensor $\epsilon(w)$ through Hooke's law,

$$\sigma(w) = \mathbb{D} : \epsilon(w)$$

where \mathbb{D} is the constitutive operator, “ $:$ ” is the double contraction of tensors, and ϵ is the symmetric strain tensor given by,

$$\epsilon(\mathbf{w}) = \frac{1}{2} (\nabla \mathbf{w} + \nabla \mathbf{w}^T)$$

63 The “material” properties for the mesh are chosen to tailor the mesh deformation, and need
 64 not represent the actual material being modeled Amar2016.

65 For the pseudo-elasticity equations, the surface velocity due to the ablating material is a
 66 function of the surface temperature $T_q(x, t)$ for $x \in \Gamma_q$ on the heated boundary. For the i -th
 67 material component, the surface velocity is imposed based on the following relation,

$$\hat{\mathbf{n}} \cdot \mathbf{v}(x, t) = f(T_q(x, t)), \quad x \in \Gamma_q \quad (3)$$

68 where $\hat{\mathbf{n}}$ is the unit normal vector on the heated boundary Γ_q , and f is a function obtained
 69 from tabulated data for the material, commonly referred to as a B’ table. The B’ table
 70 provides the recession velocity as a function of surface temperature, and is pre-computed
 71 based on high-fidelity simulations of the ablation process for a one-dimensional slab of the
 72 material, and is independent of the TPS geometry and boundary conditions. The surface
 73 displacements are then computed by integrating the surface velocities over time,

$$\mathbf{w}_q(x, t) = \int_0^t \mathbf{v}(x, \tau) d\tau = \int_0^t f(T_q(x, \tau)) d\tau \quad (4)$$

74 2.2 Full-Order Model: Finite-Element Method

75 To obtain the full-order numerical solution, the governing equation is spatially discretized
 76 using variational principles of Discontinuous Galerkin (DG) to result in a high-dimensional
 77 system of ordinary differential equations (ODEs). Note that the choice of DG approach here
 78 is mainly for theoretical convenience in the coarse-graining formulation, and is exclusively
 79 performed on the energy equation as the quantities of interest correspond to the ablating
 80 surface temperatures. In Sec. x, the high-fidelity ablating TPS solution is performed using
 81 standard FEM for both the energy and elasticitiy equations, and the equivalence between
 82 DG and standard FEM is noted upon their convergence.

83 Consider a conforming mesh partition domain, where each element belongs to one and
 84 only one component. Denote the collection of all M elements as $\{E_i\}_{i=1}^M$. In an element E_i ,
 85 its shared boundaries with another element E_j , Neumann BC, and Dirichlet BC are denoted
 86 as e_{ij} , e_{iq} , and e_{iT} , respectively. Lastly, $|e|$ denotes the length ($n_d = 2$) or area ($n_d = 3$) of a
 87 component boundary e .

88 For the i -th element, use a set of P trial functions, such as polynomials, to represent the
 89 temperature distribution,

$$T^{(i)}(x, t) = \sum_{l=1}^P \phi_l^{(i)}(x) u_l^{(i)} \equiv \boldsymbol{\phi}^{(i)}(x)^T \mathbf{u}^{(i)}(t), \quad i = 1, 2, \dots, M \quad (5)$$

90 By standard variational processes, e.g., Cohen2018, the element-wise governing equation is
 91 denoted as,

$$\mathbf{A}^{(i)} \dot{\mathbf{u}}^{(i)} = (\mathbf{B}^{(i)} + \mathbf{C}^{(i)}) \mathbf{u}^{(i)} + \sum_{j \in \mathcal{N}_i \cup \{T_b\}} \left(\mathbf{B}_{ij}^{(i)} \mathbf{u}^{(i)} + \mathbf{B}_{ij}^{(j)} \mathbf{u}^{(j)} \right) + \mathbf{f}^{(i)}(t), \quad \text{for } i = 1, 2, \dots, M \quad (6)$$

92 which is collected as the following ODE for all the elements in the mesh,

$$\mathbf{A}(\mathbf{u}) \dot{\mathbf{u}} = [\mathbf{B}(\mathbf{u}) + \mathbf{C}(\mathbf{u})] \mathbf{u} + \mathbf{f}(t) \quad (7)$$

93 where $\mathbf{u} = [\mathbf{u}^{(1)}, \mathbf{u}^{(2)}, \dots, \mathbf{u}^{(M)}]^T \in \mathbb{R}^{MP}$ includes all the DG variables, $\mathbf{f} \in \mathbb{R}^{MP}$ is the
 94 external forcing, and the system matrices \mathbf{A} , \mathbf{B} , and \mathbf{C} are the matrices due to heat capacity,
 95 heat conduction, and temperature advection due to mesh motion, respectively. A detailed
 96 derivation of eqs. (6) and (7) and their matrices is provided in Appendix [?].

97 2.3 Reduced-Physics Model

98 The RPM for predicting the response of the ablating TPS consists of two components: (1) the
 99 LCM, and (2) tabulated data for ablating velocity as a function of surface temperature. The
 100 LCM is described as a first-order system of ODEs for predicting the average temperatures
 101 inside the ablating TPS, and provides a low-fidelity under-estimation for the ablating surface
 102 temperature. The temperature prediction from LCM is used in a B' table to determine the
 103 surface recession velocity, from which the displacements are obtained through integration.

104 2.3.1 Lumped Capacitance Model

105 The main results regarding the LCM are provided in this section; details of the implementa-
 106 tion for the TPS in Fig. 2 are provided in Appendix A. The LCM is a classical physics-based
 107 low-order model for predicting the temporal variation of average temperature in multiple in-
 108 terconnected components INCROPERA. The LCM is derived at the component level from
 109 a point of view of energy conservation, and leads to the following system of ODEs for the
 110 average temperatures on the components,

$$\bar{\mathbf{A}} \dot{\bar{\mathbf{u}}} = \bar{\mathbf{B}}(\bar{\mathbf{u}}) \bar{\mathbf{u}} + \bar{\mathbf{f}}(t) \quad (8)$$

111 where,

$$\bar{\mathbf{u}} = [\bar{u}^{(1)}, \bar{u}^{(2)}, \dots, \bar{u}^{(N)}]^T \in \mathbb{R}^N \quad (9a)$$

$$\bar{\mathbf{f}} = [\bar{f}^{(1)}, \bar{f}^{(2)}, \dots, \bar{f}^{(N)}]^T \in \mathbb{R}^N \quad (9b)$$

112 includes the average temperatures $\bar{\mathbf{u}}$ and forcing inputs $\bar{\mathbf{f}}$ for the N components. For $i, j =$
113 $1, 2, \dots, N$ the (i, j) -th elements of the $\bar{\mathbf{A}} \in \mathbb{R}^{N \times N}$, $\bar{\mathbf{B}} \in \mathbb{R}^{N \times N}$, and $\bar{\mathbf{f}} \in \mathbb{R}^N$ matrices are
114 given by,

$$\bar{A}^{(i)} = \begin{cases} \int_{\Omega^{(i)}} \rho c_p d\Omega^{(i)}, & i = j \\ 0, & i \neq j \end{cases}, \quad \bar{B}_{ij} = \begin{cases} \sum_{j \in \mathcal{N}_i \cup \{T_b\}} \bar{B}_{ij}^{(i)}, & i = j \\ \bar{B}_{ij}^{(j)}, & i \neq j \end{cases}, \quad (10a)$$

$$\mathbf{f}^{(i)} = \begin{cases} |e_{iq}| \bar{q}^{(i)} + \frac{|e_{iT}|}{R_i} \bar{T}^{(i)}, & i = j \\ 0, & i \neq j \end{cases} \quad (10b)$$

115 where,

$$\bar{q}^{(i)} = \frac{1}{|e_{iq}|} \int_{e_{iq}} q_b de_{iq}, \quad \bar{T}^{(i)} = \frac{1}{|e_{iT}|} \int_{e_{iT}} T_b de_{iT}, \quad \bar{B}_{ij}^{(i)} = -\frac{|e_{ij}|}{R_{ij}}, \quad \bar{B}_{ij}^{(j)} = \frac{|e_{ij}|}{R_{ij}} \quad (11)$$

116 2.3.2 Surface Recession Velocity and Displacements

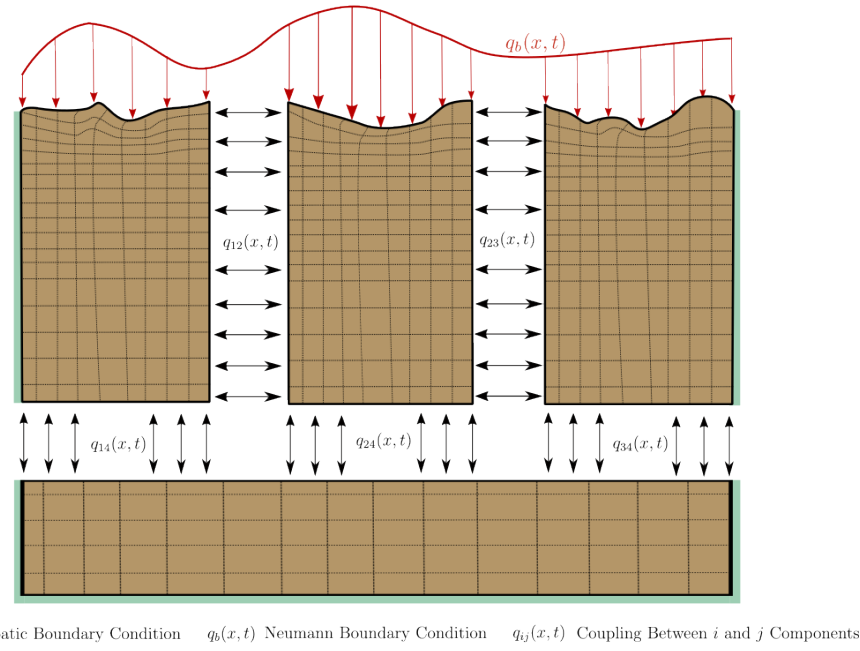
117 The surface velocity on the heated boundary Γ_q is computed based on the temperature
118 predicted by the LCM using eq. (3). Thus, based on the i -th average temperature $\bar{u}^{(i)}$, the
119 wall-normal surface velocity is computed as,

$$\hat{\mathbf{n}} \cdot \mathbf{v}^{(i)}(x, t) = f(\bar{u}^{(i)}(t)) \quad (12)$$

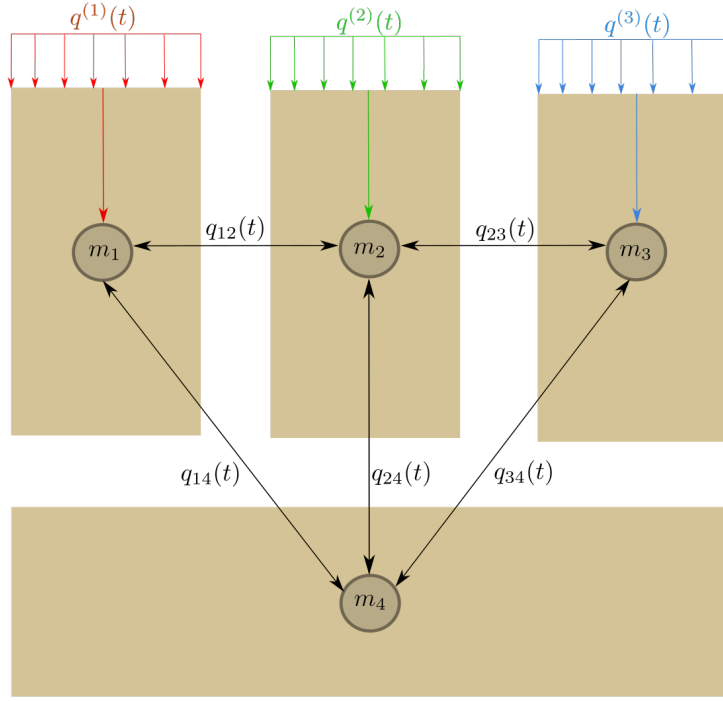
120 Due

121 2.4 Summary of Modeling Approaches

122 The FOM (i.e., DG-FEM) and RPM (i.e., LCM) are two different but mathematically con-
123 nected solution strategies. Specifically, the LCM in eq. (8) not only resembles the functional
124 form of the DG model in eq. (7), but can be viewed as a special case of the latter, where the
125 mesh partition is extremely coarse, and the trial and test functions are piece-wise constants.
126 For example, consider the case where each component $\Omega^{(i)}$ is treated as one single element,
127 and each element employs one constant basis function $\phi^{(i)} = 1$. The element-wise DG model



(a) TPS Decomposition



(b) Lumped Mass Representation

Figure 2: Partition of the TPS into three ablating and one non-ablating components with the corresponding lumped-mass representation.

128 in eq. (6) simplifies into a scalar ODE that ignores advection effects due to mesh motion,

$$\mathbf{A}^{(i)} = \bar{A}^{(i)}, \quad \mathbf{C}^{(i)} = 0, \quad \mathbf{B}_{ij}^{(i)} = -\sigma|e_{ij}|, \quad \mathbf{B}_{ij}^{(j)} = \sigma|e_{ij}|, \quad \mathbf{f}^{(i)} = |e_{iq}|\bar{q}^{(i)} + \sigma|e_{iT}|\bar{T}^{(i)} \quad (13)$$

129 Clearly, the LCM is a coarse zeroth-order DG model with the inverse of thermal resistance
130 chosen as the element-wise penalty factors. Or conversely, the DG model is a refined version
131 of LCM via *hp*-adaptation.

132 The FOM and RPM represent two extremes in the modeling fidelity and computational
133 cost spectrum. On one hand, the FOM is the most accurate but computationally expensive
134 to evaluate due to the fine mesh discretizations for both the temperature and displacement
135 fields, leading to possibly millions of state variables. On the other hand, the RPM considers
136 only the average temperature of the material as the state variable, considerably reducing
137 the computational cost, but sacrificing local temperature information and thus neglecting
138 higher-order effects due to mesh motion. Thus, neither the FOM nor the RPM is a universal
139 approach for real-world analysis, design, and optimization tasks for ablating TPS, where
140 thousands of high-fidelity model evaluations may be necessary. This issue motivates the
141 development of the PIROM, which can achieve the fidelity of FOM at a computational cost
142 close to the RPM, while maintaining the generalizability to model parameters.

143 3 Physics-Infused Reduced-Order Modeling

144 The formulation of PIROM for ablating TPS starts by connecting the FOM, i.e., DG-FEM,
145 and the RPM, i.e., the LCM, via a coarse-graining procedure. This procedure pinpoints
146 the missing dynamics in the LCM when compared to DG-FEM. Subsequently, the Mori-
147 Zwanzig (MZ) formalism is employed to determine the model form for the missing dynamics
148 in PIROM. Lastly, the data-driven identification of the missing dynamics in PIROM is
149 presented.

150 3.1 Deriving the Reduced-Physics Model via Coarse-Graining

151 The LCM is derived from a full-order DG on a fine mesh via coarse graining. This pro-
152 cess constraints the trial function space of a full-order DG model to a subset of piece-wise
153 constants, so that the variables \mathbf{u} , matrices \mathbf{A} , \mathbf{B} , and \mathbf{C} , and forcing vector \mathbf{f} are all ap-
154 proximated using a single state associated to the average temperature. The details of the
155 projection are described next.

¹⁵⁶ **3.1.1 Coarse-Graining of States**

¹⁵⁷ Consider a DG model as in eq. (7) for M elements and an LCM as in eq. (8) for N components;
¹⁵⁸ clearly $M \gg N$. Let $\mathcal{V}_j = \{i | E_i \in \Omega_j\}$ be the indices of the elements belonging to the j -th
¹⁵⁹ component, so $E_i \in \Omega_j$ for all $i \in \mathcal{V}_j$. The number of elements in the j -th component is $|\mathcal{V}_j|$.
¹⁶⁰ The average temperature on Ω_j is,

$$\bar{u}_j = \frac{1}{|\Omega_j|} \sum_{i \in \mathcal{V}_j} \int_{E^{(i)}} \phi^{(i)}(x)^T \mathbf{u}^{(i)} d\Omega = \frac{1}{|\Omega_j|} \sum_{i \in \mathcal{V}_j} |E_i| \boldsymbol{\varphi}_i^{j\top} \mathbf{u}^{(i)}, \quad j = 1, 2, \dots, N \quad (14)$$

¹⁶¹ where $|\Omega_j|$ and $|E_i|$ denote the area ($d = 2$) or volume ($d = 3$) of component j and element
¹⁶² i , respectively. The orthogonal basis functions are defined as $\boldsymbol{\varphi}_i^{j\top} = [1, 0, \dots, 0]^\top \in \mathbb{R}^P$.

¹⁶³ Conversely, given the average temperatures of the N components, $\bar{\mathbf{u}}$, the states of an
¹⁶⁴ arbitrary element E_i is written as,

$$\mathbf{u}^{(i)} = \sum_{k=1}^N \boldsymbol{\varphi}_i^k \bar{u}_k + \delta \mathbf{u}^{(i)}, \quad i = 1, 2, \dots, M \quad (15)$$

¹⁶⁵ where $\boldsymbol{\varphi}_i^k = 0$ if $i \notin \mathcal{V}_k$, and $\delta \mathbf{u}^{(i)}$ represents the deviation from the average temperature and
¹⁶⁶ satisfies the orthogonality condition $\boldsymbol{\varphi}_i^{k\top} \delta \mathbf{u}^{(i)} = 0$ for all k .

¹⁶⁷ Equations eqs. (14) and (15) are combined and written in matrix form as,

$$\bar{\mathbf{u}} = \Phi^+ \mathbf{u}, \quad \mathbf{u} = \Phi \mathbf{u} + \delta \mathbf{u} \quad (16)$$

¹⁶⁸ where $\Phi \in \mathbb{R}^{MP \times N}$ is a matrix of $M \times N$ blocks, with the (i, j) -th block as $\boldsymbol{\varphi}_i^j$, $\Phi^+ \in \mathbb{R}^{N \times MP}$
¹⁶⁹ is the left inverse of Φ , with the (i, j) -th block as $\boldsymbol{\varphi}_i^{j+} = \frac{|E_i|}{|\Omega_j|} \boldsymbol{\varphi}_i^{j\top}$, and $\delta \mathbf{u}$ is the collection of
¹⁷⁰ deviations. By their definitions, $\Phi^+ \Phi = \mathbf{I}$ and $\Phi^+ \delta \mathbf{u} = \mathbf{0}$.

¹⁷¹ **3.1.2 Coarse-Graining of Dynamics**

¹⁷² Next, consider a function of states in the form of $\mathbf{M}(\mathbf{u}) \mathbf{g}(\mathbf{u})$, where $\mathbf{g} : \mathbb{R}^{MP} \rightarrow \mathbb{R}^{MP}$
¹⁷³ is a vector-valued function, and $\mathbf{M} : \mathbb{R}^{MP} \rightarrow \mathbb{R}^{p \times MP}$ is a matrix-valued function with an
¹⁷⁴ arbitrary dimension p . Define the projection matrix $\mathbf{P} = \Phi \Phi^+$ and the projection operator
¹⁷⁵ \mathcal{P} as,

$$\begin{aligned} \mathcal{P} [\mathbf{M}(\mathbf{u}) \mathbf{g}(\mathbf{u})] &= \mathbf{M}(\mathbf{P} \mathbf{u}) \mathbf{g}(\mathbf{P} \mathbf{u}) \\ &= \mathbf{M}(\Phi \bar{\mathbf{u}}) \mathbf{g}(\Phi \bar{\mathbf{u}}) \end{aligned} \quad (17)$$

¹⁷⁶ so that the resulting function depends only on the average temperatures $\bar{\mathbf{u}}$. Correspondingly,
¹⁷⁷ the residual operator $\mathcal{Q} = \mathcal{I} - \mathcal{P}$, and $\mathcal{Q}[\mathbf{M}(\mathbf{u})\mathbf{g}(\mathbf{u})] = \mathbf{M}(\mathbf{u})\mathbf{g}(\mathbf{u}) - \mathbf{M}(\Phi\bar{\mathbf{u}})\mathbf{g}(\Phi\bar{\mathbf{u}})$. When
¹⁷⁸ the function is not separable, the projection operator is simply defined as $\mathcal{P}[\mathbf{g}(\mathbf{u})] = \mathbf{g}(\mathbf{P}\mathbf{u})$.

¹⁷⁹ Subsequently, the operators defined above are applied to coarse-grain the dynamics. First,
¹⁸⁰ write the DG-FEM in eq. (7) as,

$$\dot{\mathbf{u}} = \mathbf{A}(\mathbf{u})^{-1}\mathbf{B}(\mathbf{u})\mathbf{u} + \mathbf{A}(\mathbf{u})^{-1}\mathbf{C}(\mathbf{u})\mathbf{u} + \mathbf{A}(\mathbf{u})^{-1}\mathbf{f}(t) \quad (18)$$

¹⁸¹ and multiply both sides by Φ^+ to obtain,

$$\Phi^+\dot{\mathbf{u}} = \Phi^+(\Phi\dot{\bar{\mathbf{u}}} + \delta\dot{\mathbf{u}}) = \dot{\bar{\mathbf{u}}} = \Phi^+\mathbf{r}(\mathbf{u}, t) \quad (19)$$

¹⁸² Apply the projection operator \mathcal{P} and the residual operator \mathcal{Q} to the right-hand side to obtain,

$$\dot{\bar{\mathbf{u}}} = \mathcal{P}[\Phi^+\mathbf{r}(\mathbf{u}, t)] + \mathcal{Q}[\Phi^+\mathbf{r}(\mathbf{u}, t)] \equiv \mathbf{r}^{(1)}(\mathbf{u}, t) + \mathbf{r}^{(2)}(\mathbf{u}, t) \quad (20)$$

¹⁸³ where $\mathbf{r}^{(1)}(\mathbf{u}, t)$ is resolved dynamics that depends on $\bar{\mathbf{u}}$ only, and $\mathbf{r}^{(2)}(\mathbf{u}, t)$ is the un-resolved
¹⁸⁴ or residual dynamics. Detailed derivations and analysis of $\mathbf{r}^{(1)}(\mathbf{u}, t)$ and $\mathbf{r}^{(2)}(\mathbf{u}, t)$ can be
¹⁸⁵ found in the Appendix.

¹⁸⁶ It follows from Ref. [x](#) that the resolved dynamics is exactly the LCM, where the advection
¹⁸⁷ term reduces to zero, i.e., $\bar{\mathbf{C}}(\bar{\mathbf{u}}) = \mathbf{0}$ as shown in the Appendix. Using the notation from
¹⁸⁸ eq. (8), it follows that,

$$\begin{aligned} \mathbf{r}^{(1)}(\mathbf{u}, t) &= \bar{\mathbf{A}}(\bar{\mathbf{u}})^{-1}\bar{\mathbf{B}}(\bar{\mathbf{u}})\bar{\mathbf{u}} + \bar{\mathbf{A}}(\bar{\mathbf{u}})^{-1}\bar{\mathbf{C}}(\bar{\mathbf{u}})\bar{\mathbf{u}} + \bar{\mathbf{A}}(\bar{\mathbf{u}})^{-1}\bar{\mathbf{f}}(\bar{\mathbf{u}}) \\ &= \bar{\mathbf{A}}(\bar{\mathbf{u}})^{-1}\bar{\mathbf{B}}(\bar{\mathbf{u}})\bar{\mathbf{u}} + \bar{\mathbf{A}}(\bar{\mathbf{u}})^{-1}\bar{\mathbf{f}}(t) \end{aligned} \quad (21)$$

¹⁸⁹ where the following relations hold,

$$\bar{\mathbf{A}}(\bar{\mathbf{u}}) = \mathbf{W}(\Phi^+\mathbf{A}(\Phi\bar{\mathbf{u}})^{-1}\Phi)^{-1} \quad \bar{\mathbf{C}}(\bar{\mathbf{u}}) = \mathbf{0} \quad (22a)$$

$$\bar{\mathbf{B}}(\bar{\mathbf{u}}) = \mathbf{W}\Phi^+\mathbf{B}(\Phi\bar{\mathbf{u}})\Phi \quad \bar{\mathbf{f}}(t) = \mathbf{W}\Phi^+\mathbf{f} \quad (22b)$$

¹⁹⁰ where $\mathbf{W} \in \mathbb{R}^{N \times N}$ is a diagonal matrix with the i -th element as $[\mathbf{W}]_{ii} = |\mathcal{V}_k|$ if $i \in$
¹⁹¹ \mathcal{V}_k . As shown in the Appendix, the examination of the second residual term $\mathbf{r}^{(2)}(\mathbf{u}, t)$ in
¹⁹² eq. (20) reveals the physical sources of missing dynamics in the LCM: the approximation of
¹⁹³ non-uniform temperature within each component as a constant, and the elimination of the
¹⁹⁴ advection term due to coarse-graining.

¹⁹⁵ In sum, the above results not only show that the LCM is a result of coarse-graining of

¹⁹⁶ the full-order DG-FEM, but also reveal the discrepancies between the LCM and the DG-
¹⁹⁷ FEM. In the subsequent section, the discrepancies will be corrected to produce the proposed
¹⁹⁸ PIROM.

¹⁹⁹ 3.2 Formulation of Reduced-Order Model

²⁰⁰ The Mori-Zwanzig (MZ) formalism is an operator-projection technique used to derive ROMs
²⁰¹ for high-dimensional dynamical systems, especially in statistical mechanics and fluid dynam-
²⁰² ics Parish,Duraisamy . It provides an exact reformulation of the full-order dynamics in terms
²⁰³ of a subset of resolved variables. The proposed ROM is subsequently developed based on
²⁰⁴ such reformulation. Equation eq. (20) shows that the DG-FEM dynamics can be decomposed
²⁰⁵ into the resolved dynamics $\mathbf{r}^{(1)}(\mathbf{u}, t)$ and the orthogonal dynamics $\mathbf{r}^{(2)}(\mathbf{u}, t)$, in the sense of
²⁰⁶ $\mathcal{P}\mathbf{r}^{(2)} = 0$. In this case, the MZ formalism can be invoked to express the dynamics $\dot{\bar{\mathbf{u}}}$ in terms
²⁰⁷ of $\bar{\mathbf{u}}$ alone as the projected Generalized Langevin Equation (GLE) Parish,Duraisamy ,

$$\dot{\bar{\mathbf{u}}}(t) = \mathbf{r}^{(1)}(\bar{\mathbf{u}}, t) + \int_0^t \tilde{\boldsymbol{\kappa}}(t, s, \bar{\mathbf{u}}) ds \quad (23)$$

²⁰⁸ where the first term is Markovian, and the integral term is referred to as the memory. The
²⁰⁹ integral term is non-Markovian, accounting for impact of past resolved states on the current
²¹⁰ states through their interactions with the un-resolved states.

²¹¹ Next, to further inform the subsequent derivation of the ROM, the kernel $\tilde{\mathbf{k}}$ is examined
²¹² via a leading-order expansion, based on prior work x; this can be viewed as an analog of
²¹³ zeroth-order holding in linear system theory with a sufficiently small time step. In this case,
²¹⁴ the memory kernel is approximated as,

$$\tilde{\boldsymbol{\kappa}}(t, s, \bar{\mathbf{u}}) \approx \mathbf{r}^{(1)}(\bar{\mathbf{u}}, t) \cdot \nabla_{\bar{\mathbf{u}}} \mathbf{r}^{(2)}(\Phi \bar{\mathbf{u}}, t) \quad (24)$$

²¹⁵ Note that the terms in $\mathbf{r}^{(1)}$ have a common factor $\bar{\mathbf{A}}^{-1}$; this motivates the following heuristic
²¹⁶ modification of the model form in eq. (23),

$$\dot{\bar{\mathbf{u}}} = \mathbf{r}^{(1)}(\bar{\mathbf{u}}, t) + \bar{\mathbf{A}}^{-1}(\bar{\mathbf{u}}) \int_0^t \boldsymbol{\kappa}(t, s, \bar{\mathbf{u}}) ds \quad (25a)$$

$$\bar{\mathbf{A}}(\bar{\mathbf{u}})\dot{\bar{\mathbf{u}}} = \bar{\mathbf{B}}(\bar{\mathbf{u}})\bar{\mathbf{u}} + \bar{\mathbf{f}}(t) + \int_0^t \boldsymbol{\kappa}(t, s, \bar{\mathbf{u}}) ds \quad (25b)$$

²¹⁷ where the original kernel $\tilde{\boldsymbol{\kappa}}$ is effectively normalized by $\bar{\mathbf{A}}^{-1}$. Intuitively, such choice of kernel
²¹⁸ reduces its dependency on the averaged material properties, and simplifies the subsequent
²¹⁹ design of model form.

220 Subsequently, the hidden states are introduced to “Markovianize” the system eq. (23).
 221 In this manner, eq. (25b) is converted into a pure state-space model, with the functional
 222 form of the LCM retained; since LCM is a physics-based model, then it encodes the phys-
 223 ical information and retains explicit parametric dependence of the problem. Consider the
 224 representation of the kernel as a finite sum of simpler functions, e.g., exponentials,

$$\kappa(t, s, \bar{\mathbf{u}}) = \sum_{j=1}^m \mathcal{K}_j(t, s, \bar{\mathbf{u}}) [\mathbf{p}_j + \mathbf{d}_j(\bar{\mathbf{u}})] \phi_j(s, \bar{\mathbf{u}}) \quad (26)$$

225 where,

$$\mathcal{K}_j(t, s, \bar{\mathbf{u}}) = e^{-\int_s^t (\lambda_j + e_j(\bar{\mathbf{u}})) d\tau}, \quad \phi_j(s, \bar{\mathbf{u}}) = \mathbf{q}_j^\top \bar{\mathbf{u}}(s) + \mathbf{g}_j(\bar{\mathbf{u}})^\top \bar{\mathbf{u}}(s) + \mathbf{r}_j^\top \bar{\mathbf{f}}(s) \quad (27)$$

226 with suitable coefficients $\mathbf{p}_j, \mathbf{d}_j, \mathbf{q}_j, \mathbf{g}_j, \mathbf{r}_j \in \mathbb{R}^N$ and decay rates $\lambda_j, e_j(\bar{\mathbf{u}}) > 0$, that need to
 227 be identified from data.

228 Define the hidden states as,

$$\beta_j(t) = \int_0^t \mathcal{K}_j(s, \bar{\mathbf{u}}) \phi_j(s, \bar{\mathbf{u}}) ds \quad (28)$$

229 then through its differentiation with respect to time,

$$\dot{\beta}_j(t) = -[\lambda_j + e_j(\bar{\mathbf{u}})] \beta_j(t) + \mathbf{q}_j^\top \bar{\mathbf{u}}(t) + \mathbf{g}_j(\bar{\mathbf{u}})^\top \bar{\mathbf{u}}(t) + \mathbf{r}_j^\top \bar{\mathbf{f}}(t) \quad (29)$$

230 and the memory term becomes,

$$\int_0^t \kappa(t, s, \bar{\mathbf{u}}) ds = \sum_{j=1}^m [\mathbf{p}_j + \mathbf{d}_j(\bar{\mathbf{u}})] \beta_j(t) \quad (30)$$

231 Then, eq. (25b) is recast as the extended Markovian system,

$$\bar{\mathbf{A}}(\bar{\mathbf{u}}) \dot{\bar{\mathbf{u}}} = \bar{\mathbf{B}}(\bar{\mathbf{u}}) \bar{\mathbf{u}} + [\mathbf{P} + \mathbf{D}(\bar{\mathbf{u}})] \boldsymbol{\beta} + \bar{\mathbf{f}}(t) \quad (31a)$$

$$\dot{\boldsymbol{\beta}} = [-\boldsymbol{\Lambda} + \mathbf{E}(\bar{\mathbf{u}})] \boldsymbol{\beta} + [\mathbf{Q} + \mathbf{G}(\bar{\mathbf{u}})] \bar{\mathbf{u}} + \mathbf{R} \bar{\mathbf{f}}(t) \quad (31b)$$

²³² where,

$$\boldsymbol{\Lambda} = \text{diag}(\lambda_1, \lambda_2, \dots, \lambda_m) \in \mathbb{R}^{m \times m}, \quad \mathbf{P} = [\mathbf{p}_1, \mathbf{p}_2, \dots, \mathbf{p}_m] \in \mathbb{R}^{N \times m} \quad (32a)$$

$$\mathbf{D}(\bar{\mathbf{u}}) = [\mathbf{d}_1(\bar{\mathbf{u}}), \mathbf{d}_2(\bar{\mathbf{u}}), \dots, \mathbf{d}_m(\bar{\mathbf{u}})] \in \mathbb{R}^{N \times m}, \quad \mathbf{Q} = [\mathbf{q}_1, \mathbf{q}_2, \dots, \mathbf{q}_m] \in \mathbb{R}^{m \times N} \quad (32b)$$

$$\mathbf{G}(\bar{\mathbf{u}}) = [\mathbf{g}_1(\bar{\mathbf{u}}), \mathbf{g}_2(\bar{\mathbf{u}}), \dots, \mathbf{g}_m(\bar{\mathbf{u}})] \in \mathbb{R}^{m \times N}, \quad \mathbf{R} = [\mathbf{r}_1, \mathbf{r}_2, \dots, \mathbf{r}_m] \in \mathbb{R}^{m \times N} \quad (32c)$$

$$\mathbf{E}(\bar{\mathbf{u}}) = \text{diag}(e_1(\bar{\mathbf{u}}), e_2(\bar{\mathbf{u}}), \dots, e_m(\bar{\mathbf{u}})) \in \mathbb{R}^{m \times m} \quad (32d)$$

²³³ Since the hidden states $\boldsymbol{\beta}$ serve as the memory, their initial conditions are set to zero, i.e.,
²³⁴ $\boldsymbol{\beta}(t_0) = \mathbf{0}$, no memory at the beginning. The physics-infused model in eq. (31b) retains the
²³⁵ structure of the LCM, while the hidden states account for missing physics through corrections
²³⁶ to the stiffness and advection matrices, as well as the forcing term.

²³⁷ Lastly, denote the collection of resolved and hidden states as $\mathbf{y} = [\bar{\mathbf{u}}, \boldsymbol{\beta}]^T \in \mathbb{R}^{n_y}$ with
²³⁸ $n_y = N + m$, then the proposed PIROM is summarized as,

$$\tilde{\mathbf{A}}\dot{\mathbf{y}} = [\tilde{\mathbf{B}} + \tilde{\mathbf{C}}] \mathbf{y} + \mathbf{H}\bar{\mathbf{f}}(t) \quad (33a)$$

$$\mathbf{z} = \mathbf{M}\mathbf{y} \quad (33b)$$

²³⁹ where,

$$\tilde{\mathbf{A}} = \begin{bmatrix} \bar{\mathbf{A}}(\bar{\mathbf{u}}) & \mathbf{O} \\ \mathbf{O} & \mathbf{I} \end{bmatrix} \in \mathbb{R}^{n_y \times n_y}, \quad \tilde{\mathbf{B}} = \begin{bmatrix} \bar{\mathbf{B}}(\bar{\mathbf{u}}) & \mathbf{P} \\ \mathbf{Q} & -\boldsymbol{\Lambda} \end{bmatrix} \in \mathbb{R}^{n_y \times n_y}, \quad \tilde{\mathbf{C}} = \begin{bmatrix} \mathbf{0} & \mathbf{D}(\bar{\mathbf{u}}) \\ \mathbf{G}(\bar{\mathbf{u}}) & \mathbf{E}(\bar{\mathbf{u}}) \end{bmatrix} \in \mathbb{R}^{n_y \times n_y}, \quad (34a)$$

$$\mathbf{H} = \begin{bmatrix} \mathbf{I} \\ \mathbf{R} \end{bmatrix} \in \mathbb{R}^{n_y \times N}, \quad \mathbf{M} \in \mathbb{R}^{n_z \times n_y} \quad (34b)$$

²⁴⁰ In eq. (33), the terms $\bar{\mathbf{A}}$, $\bar{\mathbf{B}}$, and $\bar{\mathbf{f}}$ are the LCM terms. The collection of matrices,

$$\boldsymbol{\Theta} = \{\mathbf{P}, \mathbf{D}(\bar{\mathbf{u}}), \mathbf{G}(\bar{\mathbf{u}}), \boldsymbol{\Lambda}, \mathbf{E}(\bar{\mathbf{u}}), \mathbf{Q}, \mathbf{G}(\bar{\mathbf{u}}), \mathbf{R}, \mathbf{M}\}, \in \mathbb{R}^{n_\theta} \quad (35)$$

²⁴¹ are learnable parameters to capture the memory effects. Particularly, the matrices \mathbf{P} , $\boldsymbol{\Lambda}$, \mathbf{Q} , \mathbf{R}
²⁴² are constants that need to be identified from data, and account for the effects of coarse-
²⁴³ graining on the stiffness and forcing matrices. The matrices $\mathbf{D}(\bar{\mathbf{u}})$, $\mathbf{E}(\bar{\mathbf{u}})$, $\mathbf{G}(\bar{\mathbf{u}})$ are state-
²⁴⁴ dependent matrices, and account for the effects of coarse-graining on the advection matrix.
²⁴⁵ Leveraging the DG-FEM formula for the advection matrix in eq. (44c) in the Appendix, and
²⁴⁶ noting that the mesh displacements are functions of the ablating velocity as in eq. (3), the

²⁴⁷ state-dependent matrices for the i -th component are written as,

$$\mathbf{D}^{(i)}(\bar{\mathbf{u}}) \approx f^{(i)}(\bar{u}^{(i)})\mathbf{D}^{(i)}, \quad \mathbf{E}^{(i)}(\bar{\mathbf{u}}) \approx f^{(i)}(\bar{u}^{(i)})\mathbf{E}^{(i)}, \quad \mathbf{G}^{(i)}(\bar{\mathbf{u}}) \approx f^{(i)}(\bar{u}^{(i)})\mathbf{G}^{(i)} \quad (36)$$

²⁴⁸ where $f^{(i)}(\bar{u}^{(i)})$ is the surface recession velocity function in eq. (12) for the i -th component,
²⁴⁹ and $\mathbf{D}^{(i)}, \mathbf{E}^{(i)}, \mathbf{G}^{(i)}$ are constant matrices to be identified from data. In eq. (33), \mathbf{M} is a
²⁵⁰ fully-populated matrix that extracts the observables, i.e., the surface temperatures, from
²⁵¹ the PIROM states \mathbf{y} . The PIROM incorporates explicit information on the temperature-
²⁵² dependent material properties through the LCM matrices, as well as the surface recession
²⁵³ velocity function through eq. (36). The next step is focused on identifying the unknown
²⁵⁴ parameters Θ characterizing the hidden dynamics.

²⁵⁵ 3.3 Learning the Hidden Dynamics from Data

²⁵⁶ The learning of the PIROM is achieved through a neural-ODE like approach [Chen2018](#).
²⁵⁷ For ease of presentation, consider the following compact form of the PIROM in eq. (33),

$$\mathcal{F}(\dot{\mathbf{y}}, \mathbf{y}; \boldsymbol{\xi}, \Theta) = \mathbf{0} \quad (37)$$

²⁵⁸ where $\boldsymbol{\xi}$ defines the parametrization of the problem, i.e., operating conditions, such as the
²⁵⁹ BC's, as well as the material properties. Consider a dataset of N_s high-fidelity trajectories
²⁶⁰ of observables over a time interval $[t_0, t_f]$,

$$\mathcal{D} = \left\{ \left(t_k, \mathbf{z}_{\text{HF}}^{(l)}(t_k), \boldsymbol{\xi}^{(l)} \right) \right\}_{l=1}^{N_s}, \quad k = 0, 1, \dots, K \quad (38)$$

²⁶¹ The learning problem is formulated as the following differentially-constrained problem,

$$\min_{\Theta} \quad \frac{1}{N_s} \sum_{l=1}^{N_s} \frac{1}{K} \sum_{k=0}^K \left\| \mathbf{z}_{\text{HF}}^{(l)}(t_k) - \mathbf{M}\mathbf{y}^{(l)}(t_k) \right\|_2^2 \quad (39a)$$

$$\text{s.t.} \quad \mathcal{F}(\dot{\mathbf{y}}^{(l)}, \mathbf{y}^{(l)}; \boldsymbol{\xi}^{(l)}, \Theta) = \mathbf{0}, \quad t \in [t_0, t_f], \quad l = 1, 2, \dots, N_s \quad (39b)$$

$$\mathbf{y}^{(l)}(t_0) = \mathbf{y}_0(\boldsymbol{\xi}^{(l)}), \quad l = 1, 2, \dots, N_s \quad (39c)$$

262 **A Technical Details**

263 This appendix presents the technical details of the PIROM framework applied to the TPS
264 ablation problem. The first section provides the mathematical details for the definition of
265 the DG-FEM. The second section follows the projection procedures from Ref. x, and demon-
266 strates the effects of coarse-graining on the advection matrix. The third section presents the
267 derivation of the LCM model from an energy-conservation perspective.

268 **A.1 Full-Order Model**

269 To obtain the full-order numerical solution, the governing equation is spatially discretized
270 using variational principles of Discontinuous Galerkin (DG) to result in a high-dimensional
271 system of ordinary differential equations (ODEs). The DG-FEM model is written in an
272 element-wise form, which is beneficial for subsequent derivations of the lower-order models.
273 Note that the choice of DG approach here is mainly for theoretical convenience in the sub-
274 sequent coarse-graining formulation. In the numerical results, the full-order TPS ablation
275 simulations is computed using standard FEM instead, and the equivalence between DG and
276 standard FEM is noted upon their convergence.

277 **A.1.1 Domain Discretization**

278 Consider a conforming mesh partition of the domain, as shown in Fig. DOMAIN, where each
279 element belongs to one and only one component. Denote the collection of all M elements
280 as $\{E_i\}_{i=1}^M$. To ease the description of the DG model, a graph structure is employed. The
281 elements are treated as vertices, the set of which is denoted $\mathcal{V} = \{m\}_{m=1}^M$. Two neighboring
282 elements, E_i and E_j , are connected by an edge (i, j) , and the shared boundary between them
283 is denoted e_{ij} . The collection of all edges are denoted \mathcal{E} , and \mathcal{G} is referred to as a graph.
284 In the graph, the edges are unidirected, meaning if $(i, j) \in \mathcal{E}$ then $(j, i) \in \mathcal{E}$. Furthermore,
285 denote the neighbors of the i -th element as $\mathcal{N}_i = \{j | (i, j) \in \mathcal{E}\}$. Lastly, for the ease of
286 notation, introduce two special indices: T for the boundary of an element that overlaps with
287 the Dirichlet boundary condition, and similarly q for the Neumann boundary condition.

288 **A.1.2 Weak Form of Discontinuous Galerkin Method**

289 Choosing appropriate basis functions ϕ_k and ϕ_l and using the Interior Penalty Galerkin
290 (IPG) scheme [?], the variational bilinear form for eq. (1a) is,

$$\sum_{i=1}^M a_{\epsilon,i}(\phi_k, \phi_l) = \sum_{i=1}^M L_i(\phi_k) \quad (40)$$

291 where ϵ is an user-specified parameter and,

$$a_{\epsilon,i}(\phi_k, \phi_l) = \int_{E^{(i)}} \left(\rho c_p \phi_k \frac{\partial \phi_l}{\partial t} + \nabla \phi_k \cdot (\mathbf{k} \nabla \phi_l) - \rho c_p \phi_k \mathbf{v} \cdot \nabla \phi_l \right) dE^{(i)} \quad (41a)$$

$$\begin{aligned} &= - \sum_{j \in \mathcal{N}_i \cup \{T_b\}} \int_{e_{ij}} \{ \mathbf{k} \nabla \phi_k \cdot n \} [\phi_l] de_{ij} + \epsilon \sum_{j \in \mathcal{N}_i \cup \{T_b\}} \int_{e_{ij}} \{ \mathbf{k} \nabla \phi_l \cdot n \} [\phi_k] de_{ij} \\ &\quad + \sigma \sum_{j \in \mathcal{N}_i \cup \{T_b\}} \int_{e_{ij}} [\phi_k] [\phi_l] de_{ij} \end{aligned} \quad (41b)$$

$$L_i(v) = \epsilon \sum_{j \in \mathcal{N}_i \cup \{T_b\}} \int_{e_{ij}} (\mathbf{k} \nabla \phi_l \cdot n) T_b de_{ij} + \int_{e_{iq}} \phi_k q_b de_{iq} + \sigma \int_{e_{iT}} \phi_k T_b de_{iT} \quad (41c)$$

292 In the bi-linear form above, the notations $[]$ and $\{\}$ are respectively the jumps and averages
293 at the boundary e_{ij} share by two elements E_i and E_j ,

$$[u] = u|_{E_i} - u|_{E_j}, \quad \{u\} = \frac{1}{2} \left(u|_{E_i} + u|_{E_j} \right), \quad \text{for } x \in e_{ij} = E_i \cap E_j$$

294 Furthermore, in the bi-linear form, the terms associated with σ are introduced to enforce
295 the Dirichlet boundary conditions; σ is a penalty factor whose value can depend on the size
296 of an element. Depending on the choice of ϵ , the bi-linear form corresponds to symmetric
297 IPG ($\epsilon = -1$), non-symmetric IPG ($\epsilon = 1$), and incomplete IPG ($\epsilon = 0$). All these schemes
298 are consistent with the original PDE and have similar convergence rate with respect to mesh
299 size. In the following derivations, the case $\epsilon = 0$ is chosen for the sake of simplicity.

300 **A.1.3 Discontinuous Galerkin Model**

301 Next, the DG-based model is written in an element-wise form. For the i -th element, use a
302 set of P trial functions to represent the temperature as in eq. (5). Without loss of generality,
303 the trial functions are assumed to be orthogonal, so that $\int_{E^{(i)}} \phi_k^{(i)}(x) \phi_l^{(i)}(x) dx = |E^{(i)}| \delta_{kl}$,
304 where $|E^{(i)}|$ is the area ($n_d = 2$) or volume ($n_d = 3$) of the i -th element, and δ_{kl} is the
305 Kronecker delta.

306 Using test functions same as trial functions, the dynamics $\mathbf{u}^{(i)}$ is obtained by evaluating

³⁰⁷ the element-wise bi-linear forms,

$$a_{\epsilon,i}(\phi_k^{(i)}, T^{(i)}) = L_i(\phi_k^{(i)}), \quad k = 1, 2, \dots, P \quad (42)$$

³⁰⁸ The above procedure yields,

$$\mathbf{A}^{(i)} \dot{\mathbf{u}}^{(i)} = (\mathbf{B}^{(i)} + \mathbf{C}^{(i)}(t)) \mathbf{u}^{(i)} + \sum_{j \in \mathcal{N}_i \cup \{T_b\}} \left(\mathbf{B}_{ij}^{(i)} \mathbf{u}^{(i)} + \mathbf{B}_{ij}^{(j)} \mathbf{u}^{(j)} \right) + \mathbf{f}^{(i)}(t) \quad (43)$$

³⁰⁹ where for $k, l = 1, 2, \dots, P$,

$$[\mathbf{A}^{(i)}]_{kl} = \int_{E^{(i)}} \rho c_p \phi_k^{(i)} \phi_l^{(i)} dE^{(i)} \quad (44a)$$

$$[\mathbf{B}^{(i)}]_{kl} = - \int_{E^{(i)}} (\nabla \phi_k^{(i)}) \cdot (\mathbf{k} \nabla \phi_l^{(i)}) dE^{(i)} \quad (44b)$$

$$[\mathbf{C}^{(i)}]_{kl} = \int_{E^{(i)}} \rho c_p \phi_k^{(i)} \mathbf{v}^{(i)} \cdot \nabla \phi_l^{(i)} dE^{(i)} \quad (44c)$$

$$[\mathbf{B}_{ij}^{(i)}] = \int_{e_{ij}} \left\{ \mathbf{k} \nabla \phi_k^{(i)} \cdot \hat{n} \right\} \phi_l^{(i)} - \sigma [\phi_k^{(i)}] \phi_l^{(i)} de_{ij} \quad (44d)$$

$$[\mathbf{B}_{ij}^{(j)}] = \int_{e_{ij}} - \left\{ \mathbf{k} \nabla \phi_k^{(i)} \cdot \hat{n} \right\} \phi_l^{(j)} + \sigma [\phi_k^{(i)}] \phi_l^{(j)} de_{ij} \quad (44e)$$

$$[\mathbf{f}^{(i)}]_k = \int_{e_{iq}} \phi_k^{(i)} q_b de_{iq} + \sigma \int_{e_{iT}} \phi_k^{(i)} de_{iT} \quad (44f)$$

³¹⁰ The matrices $\mathbf{A}^{(i)} \in \mathbb{R}^{P \times P}$, $\mathbf{B}^{(i)} \in \mathbb{R}^{P \times P}$, and $\mathbf{C}^{(i)} \in \mathbb{R}^{P \times P}$ are respectively the capacitance,
³¹¹ conductivity, and advection matrices for element i . These matrices depend on ρ , c_p , \mathbf{k} , and
³¹² \mathbf{v} , and hence can be non-linear functions of $\mathbf{u}^{(i)}$. Since the trial functions are orthogonal, if
³¹³ ρc_p is constant within an element, $\mathbf{A}^{(i)}$ is diagonal; otherwise, \mathbf{A}_i is symmetric and positive
³¹⁴ definite as $\rho c_p > 0$.

³¹⁵ For compactness, the element-wise model in eq. (43) is also written in matrix form,

$$\mathbf{A}(\dot{\mathbf{u}}) = [\mathbf{B}(\mathbf{u}) + \mathbf{C}(\mathbf{u})] \mathbf{u} + \mathbf{f}(t) \quad (45)$$

³¹⁶ where $\mathbf{u} = [\mathbf{u}^{(1)}, \mathbf{u}^{(2)}, \dots, \mathbf{u}^{(M)}]^T \in \mathbb{R}^{MP}$ includes all DG variables, $\mathbf{f} = [\mathbf{f}^{(1)}, \mathbf{f}^{(2)}, \dots, \mathbf{f}^{(M)}]^T \in \mathbb{R}^{MP}$, \mathbf{A} and \mathbf{C} are matrices of M diagonal blocks whose i -th blocks are $\mathbf{A}^{(i)}$ and $\mathbf{C}^{(i)}$, and
³¹⁷ \mathbf{B} is a matrix of $M \times M$ blocks whose (i, j) -th block is,
³¹⁸

$$\mathbf{B}_{ij} = \begin{cases} \mathbf{B}^{(i)} + \sum_{j \in \mathcal{N}_i \cup \{T_b\}} \mathbf{B}_{ij}^{(i)}, & i = j \\ \mathbf{B}_{ij}^{(j)}, & i \neq j \end{cases} \quad (46)$$

319 The dependency of \mathbf{A} , \mathbf{B} , and \mathbf{C} on \mathbf{u} is explicitly noted in eq. (45), which is the source of
320 non-linearity in the current TPS problem. Moreover, the mesh velocity \mathbf{v} varies with space
321 and time, and thus the advection matrix \mathbf{C} varies with time as a function of q_b .

322 A.2 Coarse-Graining of Dynamics

323 The LCM is obtained by coarse-graining the full-order DG-FEM. This coarse-graining proce-
324 dure produces resolved $\mathbf{r}^{(1)}(\mathbf{u}, t)$ and residual $\mathbf{r}^{(2)}(\mathbf{u}, t)$ dynamics as in eq. (20). This section
325 presents the detail derivations and magnitude analysis for the resolved and residual dynam-
326 ics.

327 A.2.1 Resolved Dynamics

328 Using eq. (17), the resolved dynamics is computed as follows,

$$\mathbf{r}^{(1)}(\mathbf{u}, t) = \mathcal{P} [\Phi^+ \mathbf{A}(\mathbf{u})^{-1} (\mathbf{B}(\mathbf{u})\mathbf{u} + \mathbf{C}(\mathbf{u})\mathbf{u} + \mathbf{f}(t))] \quad (47a)$$

$$\begin{aligned} &= \Phi^+ \mathbf{A}(\mathbf{Pu})^{-1} \mathbf{PB}(\mathbf{Pu}) \mathbf{Pu} + \Phi^+ \mathbf{A}(\mathbf{Pu})^{-1} \mathbf{PC}(\mathbf{Pu}) \mathbf{Pu} \\ &\quad + \Phi^+ \mathbf{A}(\mathbf{Pu})^{-1} \mathbf{Pf}(t, \mathbf{Pu}) \end{aligned} \quad (47b)$$

$$\begin{aligned} &= \underbrace{\Phi^+ \mathbf{A}(\Phi \bar{\mathbf{u}})^{-1} \Phi}_{\#1} \underbrace{\Phi^+ \mathbf{B}(\Phi \bar{\mathbf{u}}) \Phi \bar{\mathbf{u}}}_{\#2} + \Phi^+ \mathbf{A}(\Phi \bar{\mathbf{u}})^{-1} \Phi \underbrace{\Phi^+ \mathbf{C}(\Phi \bar{\mathbf{u}}) \Phi \bar{\mathbf{u}}}_{\#3} \\ &\quad + \Phi^+ \mathbf{A}(\Phi \bar{\mathbf{u}})^{-1} \Phi \underbrace{\Phi^+ \mathbf{f}(t, \Phi \bar{\mathbf{u}})}_{\#4} \end{aligned} \quad (47c)$$

329 Detailed derivations for the #1, #2, and #4 terms can be found in Ref. [x](#). The effects of
330 coarse-graining on the advection term #3 are analyzed next.

331 **Term #3** The $\mathbf{C}(\mathbf{u}) \in \mathbb{R}^{MP \times MP}$ matrix contains M diagonal of size $P \times P$, since the
332 basis functions are defined locally on each element. Therefore, $[\mathbf{C}(\mathbf{u})]_{ij} = \mathbf{0}$ for all $i \neq j$ with
333 $i, j = 1, 2, \dots, M$. It follows that for $k, l = 1, 2, \dots, N$,

$$[\Phi^+ \mathbf{C}(t, \Phi \bar{\mathbf{u}}) \Phi]_{kl} = \sum_{i=1}^M \sum_{j=1}^M \boldsymbol{\varphi}_i^{k+} [\mathbf{C}(t, \Phi \bar{\mathbf{u}})]_{ij} \boldsymbol{\varphi}_j^l \quad (48a)$$

$$= \sum_{i=1}^M \boldsymbol{\varphi}_i^{k+} [\mathbf{C}(t, \Phi \bar{\mathbf{u}})]_{ii} \boldsymbol{\varphi}_i^l \quad (48b)$$

$$= \sum_{i \in \mathcal{V}_k} \boldsymbol{\varphi}_i^{k+} [\mathbf{C}(t, \Phi \bar{\mathbf{u}})]_{ii} \boldsymbol{\varphi}_i^l \quad (48c)$$

³³⁴ where in the second row, the fact that $[\mathbf{C}(\mathbf{u})]_{ij} = 0$ for all $i \neq j$ is used, and in the last row,
³³⁵ the fact that $\varphi_i^{k+} = 0$ for all $i \notin \mathcal{V}_k$ is used. Now, considering that $[\mathbf{C}(\mathbf{u})]_{ii}$ has a $(1, 1)$ -th
³³⁶ zero element, i.e., $[C_{11}(t, \Phi\bar{\mathbf{u}})]_{ii} = 0$, and that if $k \neq l$ then $i \notin \mathcal{V}_l$ and thus $\varphi_i^l = \mathbf{0}$, it follows
³³⁷ that for some index $i \in \mathcal{V}_k$,

$$\varphi_i^{k+} [\mathbf{C}(t, \Phi\bar{\mathbf{u}})]_{ii} \varphi_i^l = \varphi_i^{k+} [\mathbf{C}(t, \Phi\bar{\mathbf{u}})]_{ii} \varphi_i^k = \frac{|E_i|}{|\Omega_k|} [C_{11}(t, \Phi\bar{\mathbf{u}})]_{ii} = 0 \quad (49)$$

³³⁸ The matrix $[\Phi^+ \mathbf{C}(t, \Phi\bar{\mathbf{u}}) \Phi]_{kl} = 0$ for all $k, l = 1, 2, \dots, N$, and thus,

$$\bar{\mathbf{C}}(t, \bar{\mathbf{u}}) = \Phi^+ \mathbf{C}(t, \Phi\bar{\mathbf{u}}) \Phi = \mathbf{0} \quad (50)$$

³³⁹ as indicated by the LCM in eq. (8).

³⁴⁰ A.2.2 Magnitude Analysis for Residual Dynamics

³⁴¹ Next, the magnitude of the residual dynamics $\mathbf{r}^{(2)}(\mathbf{u}, t)$ is analyzed to pinpoint the missing
³⁴² physics in the LCM. By definition,

$$\mathbf{r}^{(2)}(\mathbf{u}, t) = \dot{\bar{\mathbf{u}}} - \mathbf{r}^{(1)}(\bar{\mathbf{u}}, t) \quad (51a)$$

$$= \Phi^+ \mathbf{r}(\mathbf{u}, t) - \mathbf{r}^{(1)}(\mathbf{u}, t) \quad (51b)$$

$$\begin{aligned} &= \underbrace{\Phi^+ \mathbf{A}(\mathbf{u})^{-1} \mathbf{B}(\mathbf{u}) \mathbf{u} - \bar{\mathbf{A}}(\bar{\mathbf{u}})^{-1} \bar{\mathbf{B}}(\bar{\mathbf{u}}) \bar{\mathbf{u}}}_{\#1} + \underbrace{\Phi^+ \mathbf{A}(\mathbf{u})^{-1} \mathbf{C}(\mathbf{u}) \mathbf{u} - \bar{\mathbf{A}}(\bar{\mathbf{u}})^{-1} \bar{\mathbf{C}}(t, \bar{\mathbf{u}}) \bar{\mathbf{u}}}_{\#2} \\ &\quad + \underbrace{\Phi^+ \mathbf{A}(\mathbf{u})^{-1} \mathbf{f}(t) - \bar{\mathbf{A}}(\bar{\mathbf{u}})^{-1} \bar{\mathbf{f}}(t)}_{\#3} \end{aligned} \quad (51c)$$

³⁴³ The magnitude analysis for terms $\#1$ and $\#3$ can be found in Ref. [x](#). The analysis for term
³⁴⁴ $\#2$ is presented next. Let $\mathbf{D}(\bar{\mathbf{u}}) = \mathbf{A}(\Phi\bar{\mathbf{u}})^{-1} \mathbf{P} \mathbf{C}(t, \Phi\bar{\mathbf{u}})$, then,

$$\Phi^+ \mathbf{A}(\mathbf{u})^{-1} \mathbf{C}(\mathbf{u}) \mathbf{u} - \bar{\mathbf{A}}(\bar{\mathbf{u}})^{-1} \bar{\mathbf{C}}(t, \bar{\mathbf{u}}) \bar{\mathbf{u}} \quad (52a)$$

$$= \Phi^+ \mathbf{A}(\mathbf{u})^{-1} \mathbf{C}(\mathbf{u}) \mathbf{u} - \Phi^+ \mathbf{A}(\Phi\bar{\mathbf{u}})^{-1} \mathbf{P} \mathbf{C}(t, \Phi\bar{\mathbf{u}}) \Phi \Phi^+ \mathbf{u} \quad (52b)$$

$$= \Phi^+ \mathbf{A}^{-1}(\mathbf{u}) \mathbf{C}(\mathbf{u}) \mathbf{u} - \Phi^+ \mathbf{D}(\bar{\mathbf{u}}) \Phi \Phi^+ \mathbf{u} \quad (52c)$$

$$(52d)$$

345 where $\mathbf{P} = \Phi\Phi^+$. Thus,

$$\|\Phi^+\mathbf{A}(\mathbf{u})^{-1}\mathbf{C}(\mathbf{u})\mathbf{u} - \bar{\mathbf{A}}^{-1}(\bar{\mathbf{u}})\bar{\mathbf{C}}(t, \bar{\mathbf{u}})\bar{\mathbf{u}}\| \quad (53a)$$

$$\leq \|\Phi^+\mathbf{A}^{-1}(\mathbf{u})\mathbf{C}(\mathbf{u})\mathbf{u} - \Phi^+\mathbf{D}(\bar{\mathbf{u}})\mathbf{u}\| + \|\Phi^+\mathbf{D}(\bar{\mathbf{u}})\mathbf{u} - \Phi^+\mathbf{D}(\bar{\mathbf{u}})\Phi\Phi^+\mathbf{u}\| \quad (53b)$$

$$\leq \|\Phi^+\| \underbrace{\|\mathbf{A}^{-1}(\mathbf{u})\mathbf{C}(\mathbf{u})\mathbf{u} - \mathbf{D}(\bar{\mathbf{u}})\mathbf{u}\|}_{\#1} + \|\Phi^+\mathbf{D}(\bar{\mathbf{u}})\| \underbrace{\|\mathbf{u} - \Phi\Phi^+\mathbf{u}\|}_{\#2} \quad (53c)$$

346 where term $\#2$ is due to the appriximation of non-uniform temperaeture as constants, and
 347 term $\#1$ is the error in the advection dynamics due to coarse-graining.

348 A.3 Lumped Capacitance Model

349 The following assumptions are employed: (1) the temperature in component (i) is described
 350 by a scalar time-varying average temperature $\bar{u}^{(i)}$, (2) between neighboring components (i)
 351 and (j) the heat flux is approximated as,

$$q_{ij} = \frac{\bar{u}^{(j)} - \bar{u}^{(i)}}{R_{ij}} \quad (54)$$

352 where R_{ij} is the thermal resistance. Empirically, for a component of isotropic heat conduc-
 353 tivity k , length ℓ , and cross-section area A , the thermal resistance is $R = \ell/kA$. Between
 354 components i and j , define $R_{ij} = R_i + R_j$. In addition, the heat flux due to Dirichlet
 355 boundary condition is computed as $q_{iT} = (T_b - \bar{u}^{(i)})/R_i$.

356 At component i , the dynamics of LCM are given by,

$$\int_{E^{(i)}} \rho c_p \dot{\bar{u}}^{(i)} dE^{(i)} = \left(\sum_{j \in \mathcal{N}_i} \int_{e_{ij}} \frac{\bar{u}^{(j)} - \bar{u}^{(i)}}{R_{ij}} de_{ij} \right) + \int_{e_{iq}} q_b de_{iq} + \int_{e_{iT}} \frac{T_b - \bar{u}^{(i)}}{R_i} de_{iT} \quad (55a)$$

$$\bar{A}^{(i)} \dot{\bar{u}}^{(i)} = \left(\sum_{j \in \mathcal{N}_i} \frac{|e_{ij}|}{R_{ij}} (\bar{u}^{(j)} - \bar{u}^{(i)}) \right) + |e_{iq}| \bar{q}^{(i)} + \frac{|e_{iT}|}{R_i} (\bar{T}^{(i)} - \bar{u}^{(i)}) \quad (55b)$$

$$= \sum_{j \in \mathcal{N}_i} \left(-\frac{|e_{ij}|}{R_{ij}} \bar{u}^{(i)} + \frac{|e_{ij}|}{R_{ij}} \bar{u}^{(j)} \right) + \left(-\frac{|e_{iT}|}{R_i} \bar{u}^{(i)} \right) + \left(|e_{iq}| \bar{q}^{(i)} + \frac{|e_{iT}|}{R_i} \bar{T}^{(i)} \right) \quad (55c)$$

$$= \sum_{j \in \mathcal{N}_i \cup \{T_b\}} \left(\bar{B}_{ij}^{(i)} \bar{u}^{(i)} + \bar{B}_{ij}^{(j)} \bar{u}^{(j)} \right) + \bar{f}^{(i)} \quad (55d)$$

357 where in eq. (55b) $|e|$ denotes the length ($d = 2$) or area ($d = 3$) of a component boundary
 358 e . The $\bar{A}^{(i)}$, $\bar{B}_{ij}^{(i)}$, and $\bar{B}_{ij}^{(j)}$ quantities are provided in eq. (11).

359 The lumped-mass representation for the four-component TPS is shown in Fig. 2. Let v_i

represent the area of the i -th element, $\overline{\rho c_p}_{,i}$, the heat capacity evaluated using the average temperature $\bar{u}^{(i)}$, and $1/R_{ij} = 1/R_i(\bar{u}^{(i)}) + 1/R_j(\bar{u}^{(j)})$ the equivalent thermal resistance between elements i and j . Leveraging the formulas from eqs. (10b) and (11), the LCM matrices are given by,

$$\bar{\mathbf{A}} = \begin{bmatrix} \overline{\rho c_p}_{,1} v_1 & 0 & 0 & 0 \\ 0 & \overline{\rho c_p}_{,2} v_2 & 0 & 0 \\ 0 & 0 & \overline{\rho c_p}_{,3} v_3 & 0 \\ 0 & 0 & 0 & \overline{\rho c_p}_{,4} v_4 \end{bmatrix}, \quad (56a)$$

$$\bar{\mathbf{B}} = \begin{bmatrix} \frac{1}{R_{12}} + \frac{1}{R_{14}} & -\frac{1}{R_{12}} & 0 & -\frac{1}{R_{14}} \\ -\frac{1}{R_{12}} & \frac{1}{R_{12}} + \frac{1}{R_{24}} + \frac{1}{R_{23}} & -\frac{1}{R_{23}} & -\frac{1}{R_{24}} \\ 0 & -\frac{1}{R_{32}} & \frac{1}{R_{32}} + \frac{1}{R_{34}} & -\frac{1}{R_{34}} \\ -\frac{1}{R_{14}} & -\frac{1}{R_{24}} & -\frac{1}{R_{34}} & \frac{1}{R_{14}} + \frac{1}{R_{24}} + \frac{1}{R_{34}} \end{bmatrix}, \quad \bar{\mathbf{f}} = \begin{bmatrix} \bar{q}^{(1)} \\ \bar{q}^{(2)} \\ \bar{q}^{(3)} \\ 0 \end{bmatrix} \quad (56b)$$